https://doi.org/10.5194/egusphere-2026-1163
Preprint. Discussion started: 3 July 2026


# Image Navigation Validation for FY-4A Geostationary Interferometric Infrared Sounder Using the Ground-based Laser Positioning System

Yun Cao[1,2,3], Jian Shang[1,2,3], Lei Yang[1,2,3], Hongquan Yao[4], Chengbao Liu[5], Xiaopeng Zhu[6], Xinghui Zhao[7], Pan Huang[8], Jiqiao Liu[6], Jing Wang[9], and Zhiqing Zhang[1,2,3]

[1] National Satellite Meteorological Center (National Center for Space Weather), China Meteorological Administration, Beijing 100081, China
[2] Innovation Center for FengYun Meteorological Satellite (FYSIC), China Meteorological Administration, Beijing 100081, China
[3] The Key Laboratory of Radiometric Calibration and Validation for Environmental Satellites, China Meteorological Administration, Beijing 100081, China
[4] Nanjing Zhongke ShenGuang Science and Technology Co.Ltd, Nanjing 210038, China
[5] Technology and Engineering Center for Space Utilization,Chinese Academy of Sciences, Beijing 100094, China
[6] Shanghai Institute of Optics and Fine Mechanics,Chinese Academy of Sciences, Shanghai 201800, China
[7] State Key Laboratory of Brain Cognition and Brain-inspired Intelligence Technology, Institute of Automation, Chinese Academy of Sciences, Beijing 100190, China
[8] School of Astronautics, Beihang University Beijing 100083, and with Research Institute of Intelligent Decision Engineering, CASIC, Wuhan 430040, China
[9] Institute of Software Chinese Academy of Sciences, Beijing 100190, China

*Correspondence to*: Jian Shang (shangjian@cma.gov.cn) and Lei Yang (yangl@cma.gov.cn)

**Abstract.** Accurate image navigation validation (INV) is essential for the longwave (LW) bands of the geostationary interferometric infrared sounder (GIIRS) onboard the Fengyun 4A (FY-4A) satellite. However, few scientific peer-reviewed papers have been reported to date. In this study, we present, for the first time worldwide, a satellite-ground integrated INV technique applied to the FY-4A GIIRS's LW, leveraging the ground-based laser positioning system (GLPS) to assess its navigation precision. The GLPS is designed to precisely and automatically point at the satellite and transmits laser signals whose center wavelength is predesigned and thus can be detected by GIIRS's LW detectors. Two observation modes are designed for GIIRS when the laser operations are scheduled, namely, dwell observation mode and step scanning mode. For the data analysis, three methods are proposed for different stages of data processing. A simple but universal and efficient algorithm called laser index is proposed for laser signal detection. Two customized algorithms are used for the designed laser operations to obtain the image navigation deviations in dwell observation and step scanning modes. The laser tests demonstrate that east-to-west navigation deviations are within 0.35 pixels, and north-to-south navigation deviations are within 0.45 pixels, which is consistent with the results of equivalent results from the visible band. The result analysis of the laser data demonstrates that the proposed methods are effective and precise, and it is a reliable tool to verify the image navigation results through GLPS.

https://doi.org/10.5194/egusphere-2026-1163
Preprint. Discussion started: 3 July 2026


## 1 Introduction

The GIIRS onboard the FY-4A satellite is the world's first hyperspectral infrared sounder on a geostationary platform, which can provide breakthrough measurements with high temporal, horizontal, and vertical resolution for improved nowcasting and NWP services (Yang et al., 2017; Wang et al., 2019). Verifying and validating precisely image navigation and registration performance in the post-launch period is essential and necessary for performance evaluation and long-term monitoring (Grycewicz et al., 2016; De et al., 2016).

The INV can be accessed through landmark registration and star observation. Landmark registration is a powerful way through matching the GCPs of a measured image to the corresponding GCPs extracted from a digital map (Emery et al., 2003; Yang et al., 2011; Wang et al., 2017; Hou et al., 2020). However, cloud cover usually affects landmark-based methods, causing low matching accuracy or even matching failure. Star measurements using space-borne instruments are unaffected by the cloud cover (Jiang et al., 2021; Li et al., 2019; Tan et al., 2017). They can be observed all day and in all-weather and have been widely used in the geometric correction of the geostationary high-orbit satellite. For the advanced geosynchronous radiation imager (AGRI) onboard FY-4A, the thermal deformation parameters were calculated by tracking stars to correct the pointing variations, which mitigates the influence of the thermal deformation (Shang et al., 2017; Shang et al., 2019). However, some instruments or some channels do not have star observation capabilities and cannot observe the landmarks at night, such as the LW detector of GIIRS and lightning mapping imager (LMI) onboard the FY-4A (Wang et al., 2021), causing great difficulty and challenge to the INR.

GIIRS is equipped with one visible focal plane with 2km spatial resolution and two infrared (LW and medium-wave (MW)) bands with 16km spatial resolution. All of which require accurate navigation. The visible band is navigated with landmark and star observations. However, the MW and LW bands lack effective INV capabilities. First, the infrared bands have low spatial resolution and misalignments between detectors, which greatly complicates to INV using the landmarks. Additionally, the infrared bands are unable to observe stars. Finally, GIIRS's beamsare is split into two parts: the Michelson interferometer (the key component of GIIRS for the interferogram measurement in the infrared spectral region) and the visible focal plane. Thus, the visible band and infrared bands operate on separate and independent optical paths. Due to optical misalignment, a co-registration error exists between the visible band and the MW/LW bands. It is not appropriate to use the visible band directly verifying the INR of infrared bands because of the co-registration error between the visible and infrared bands. The laser measurements can provide precise GCPs for the INV during the diurnal cycle. It provides a novel technology for the instruments that do not have star observation capabilities or cannot see landmarks at night. The GOES-16 and 17 made a preliminary attempt to demonstrate the possibility of ground-based laser measurements on the global lightning mapper (GLM) (Buechler et al., 2018). The Chinese GLPS program designed for FY-4A GIIRS in January 2016, which is almost started preparations at the same time with the ground-based laser beacons for GOES-16 GLM. FY-4A's first GLPS was completed in the December 2017, by which time the construction of the infrastructure, renovated laser laboratory and commissioning of the laser equipment had been completed. Similarly, the parameters of GLPS, such as wavelength,

https://doi.org/10.5194/egusphere-2026-1163
Preprint. Discussion started: 3 July 2026


power of the laser pulses, pulse width, power stability, signal to noise ratio (SNR) of GIIRS, have been fully demonstrated to ensure that can be detected by GIIRS's LW band (See Section 2 for details). The above researches demonstrate that laser measurement is an effective tool for INV.

Therefore, in order to verify the INR precisely, we proposed the on-orbit INV for the FY-4A GIIRS's LW band using the GLPS for the first time worldwide. The GLPS points at FY-4A satellite and continuously transmits laser signals with a wavelength of 10.59 um, which can be detected by GIIRS's LW detector. Two observation modes of GIIRS were designed when the laser operations were scheduled, namely, dwell observation and step scanning. Detecting the laser signal precisely from the observed LW data is the premise of INV. A simple but universal and efficient algorithm called laser index for laser signal detection is proposed. For each detector, the laser index is calculated from the difference between the maximum and average value that removes the maximum and sub-maximum values. Moreover, two customized algorithms are proposed to obtain the image navigation deviations in dwell observation and step scanning. The gray centroid method with the weighted matrix is applied for the dwell observation to extract the deviation of the laser signal's center compared to the ideal center. The weighted matrix is defined by the distance between the central detector and the center of its 3×3 nearest neighbor in the GIIRS's LW detector array. For the step scanning, a three-dimensional coordinate system is established. The Kriging method is applied to interpolate the discontinuous laser signals, and then the coordinate position of the most prominent laser signals in $(2n+1)^2$ images would be the subpixel deviation in the north-south (NS) and east-west (EW) directions. The result analysis of the laser data shows that the proposed three methods are effective and precise, and it is a reliable tool to verify the image navigation results through GLPS.

The main contributions of this article are as follows.

(1) A novel validation technique of the image navigation for the FY-4A GIIRS using GLPS is proposed, which is fulfilled by satellite-earth integrated observation. The parameters of GLPS, such as wavelength, SNR of GIIRS, power of the laser pulses, pulse width, power stability, have been fully demonstrated to ensure that can be detected by GIIRS's LW band.

(2) Due to the misalignments of the GIIRS's array, two observation modes are designed for GIIRS onboard, i.e., dwell observation, and step scanning, which can carry on the INV at pixel level and sub-pixel level, respectively.

(3) Three methods for analyzing the observed LW data are proposed for different stages of data processing. Firstly, a simple but efficient algorithm called laser index is proposed for laser signal detection. Two assessment methods for verifying image navigation accuracy are developed under two different observation modes based on the laser signal detection results. Preliminary results are given and geolocation accuracy is analyzed using actual observation data by GIIRS and GLPS.

## 2 Characteristics of the FY-4A GIIRS

Chinese new-generation GEO meteorological satellite FY-4 uses the advanced three-axis stabilized platform that orbits the Earth at an altitude of 35786 km in a geosynchronous orbit. GIIRS onboard FY-4A, the first satellite of the FY-4 series, is

https://doi.org/10.5194/egusphere-2026-1163
Preprint. Discussion started: 3 July 2026


the world's first hyperspectral infrared sounder on a geostationary platform. GIIRS has provided valuable observations above the equator at 104.7 ℃.

There are two mirrors perpendicularly mounted in the scanner of GIIRS, which can scan in both north-south (NS) and east-west (EW) directions. The main characteristics of GIIRS are presented in Table 1. The visible band ranges from 0.55 μm to 0.75 μm. GIIRS has 689 LW bands and 961 mid-wave (MW) bands with a spectral resolution of 0.625 $cm^{-1}$, whose LW bands range from 700 to 1130 $cm^{-1}$ and MW bands range from 1650 to 2250 $cm^{-1}$. The beamsare is spilt into two parts: one is transferred to the Michelson interferometer for the interferogram measurement in the infrared spectral region and the other is further focused onto the visible focal plane. Therefore, the visible focal plane and LW/MW focal plane are not the common path. LW and MW focal planes both have 128 detectors, while the spatial resolution of each detector is 16km at the nadir. The size of each detector is 120 μm * 120 μm. The 128 detectors are arranged into a 32*4 array with misalignments, as shown in Fig. 1. The detectors have an interval in the EW direction, while the interval between adjacent detectors is 120 μm. In the NS direction, the interval between adjacent detectors in one column is 34 μm. The first and the second columns have misplaced 77 μm, the same as the third and the fourth columns. The misalignments bring great difficulty in validating the INR performance via the GLPS.

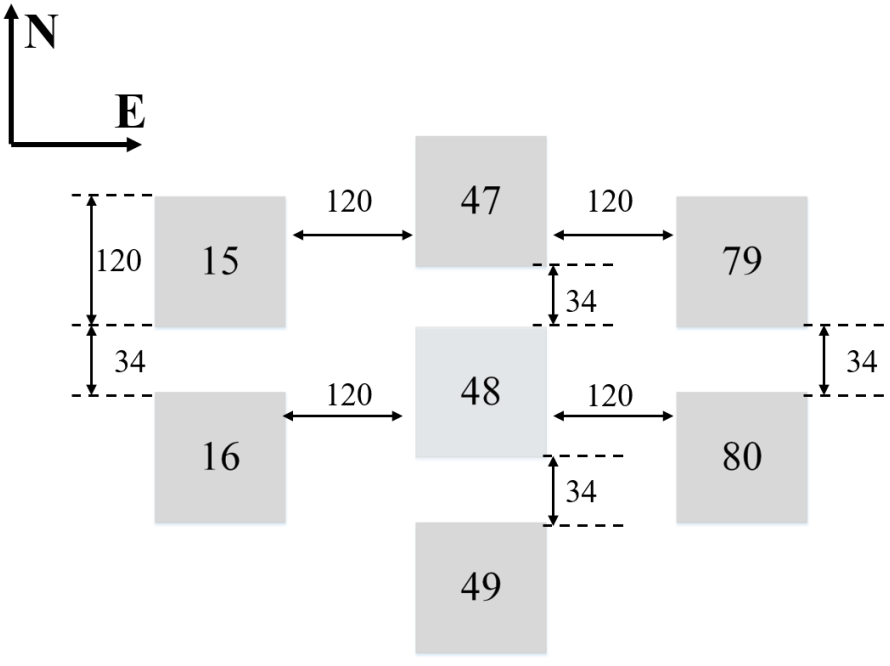


**Figure 1:** Layout of GIIRS detector array. The unit of the numbers in the figure is μm.

**Table 1.** Main characteristics of GIIRS.

| Index | Characteristics |
|---|---|

https://doi.org/10.5194/egusphere-2026-1163
Preprint. Discussion started: 3 July 2026


| | |
|---|---|
| Spectral parameter | Visible: 0.55–0.75 μm<br>LW: 1650–2250 $cm^{-1}$<br>MW: 700–1130 $cm^{-1}$ |
| Temporal resolution | 35 min (1000 km × 1000 km)<br>67 min (5000 km × 5000 km) |
| Star sensing ability | 6.5 Mv (visual magnitude) |
| Radiation calibration accuracy | 1.5 K |
| Spectrum calibration accuracy | 10 ppm |

Currently, the observation modes of the GIIRS can be divided into the following categories: region, landmark, star, laser, blackbody, cold space, and moon. For the INR, periodical star and landmark observations are necessary. The blackbody and cold space observations are essential for calibration. Routine observation tasks include region task, blackbody task, cold-space task, and star task.

## 3 Ground-based laser positioning system

### 3.1 GLPS principle

GLPS utilizes fixed stations as beacon sources to assess the INV of the GIIRS's LW band. When the GLPS stations target the satellite and shoot laser signals, the laser signal is received by the LW detector of GIIRS and forms a laser spot on it. According to the paraxial optical imaging principle, points in the object space where the ground station is located and those in the image space corresponding to the detector focal plane are mutually conjugate. Thus, the position of the laser spot centroid precisely corresponds to the object space of the ground station. The navigation accuracy can thereby be evaluated through the laser spot centroid on the detector. Since the laser station has a precise geographical location without moving, it can be used as an excellent GCP. The GLPS measurements provide unambiguous GCP and can be transmitted at whole day.

### 3.2 GLPS stations

A long continental baseline within the GIIRS's field of view (FOV) is carried out by setting up one station at Jiamusi, Heilongjiang Province, and another at Xinjiang Autonomous Region, China (See Fig.2). The primary rationale for neglecting the influence of the parallax effect is twofold. First, the two ground stations are situated at approximately similar latitudes. Second, both the dwell and step observation modes of the GIIRS are both designed to specifically orient the scanning mirror toward the ground station. Consequently, any geometric discrepancy arising from the parallax effect is considered negligible under this configuration.

https://doi.org/10.5194/egusphere-2026-1163
Preprint. Discussion started: 3 July 2026


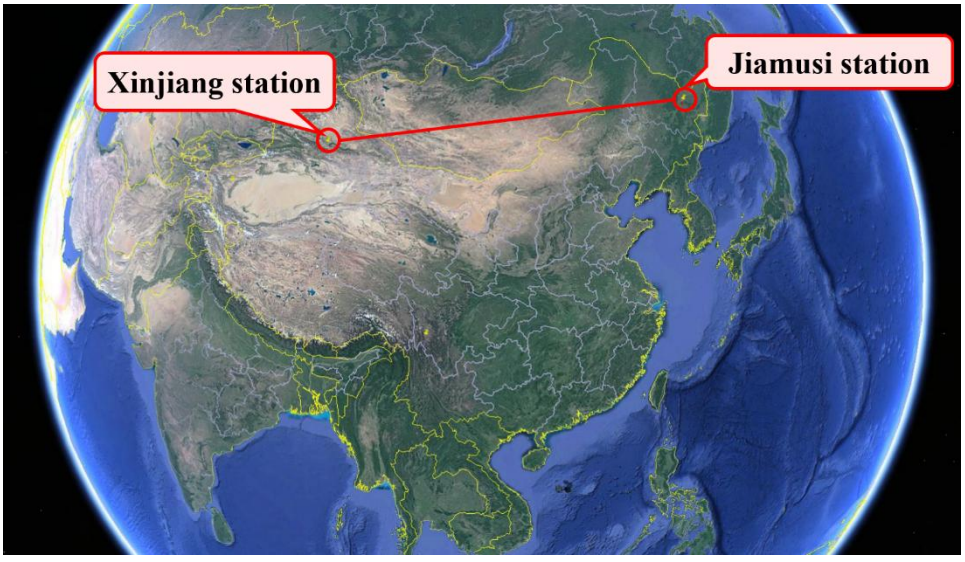


**Figure 2:** The locations of the GLPS stations are shown as circles. Base map from Baidu Maps (©Baidu).

### 3.3 GLPS Parameters

The spectral response of GIIRS's LW band is 700–1130 $cm^{-1}$. Within this spectral range, the CO2 laser is well-established, operating at a center wavelength of 10.6 μm (943.39cm-1), an average power of 300 W, and an M2 factor of less than 2. Analysis based on the Modtran database showed that the total atmospheric transmittance for the 10.6 μm laser is approximately 0.63. By integrating the emission efficiency of GLPS with the LW detector's efficiency at 10.6 μm, the signal-to-noise ratio (SNR) of LW band for GLPS has been calculated to exceed 20 under clear weather conditions. Generally speaking, the SNR over 3 can meet the LW band's detection requirements. Thus, the laser signal is capable of propagating through the atmosphere and being captured by the GIIRS's LW band.

For convenience in subsequent alignment, a laser beam at a center wavelength of 532 nm was employed as an indicator. The beams from the two lasers were spatially combined by adjusting mirrors M8, M9, M10, and M11. A Coude optical path is formed by mirrors M1 through M5. The central line defined by M1 and M2 is aligned with the elevation axis of the laser transmitting telescope, and the central line of M4 and M5 is aligned with its azimuth rotation axis. Adjustment of mirrors M6 and M7 ensures that the laser propagates strictly along the azimuth and elevation axes of the laser transmitting telescope. This ensures an invariant laser pointing direction during satellite tracking, which is a prerequisite for the detector to maintain uninterrupted reception of the ground-based laser signal. During each laser operation, systematic pointing errors can be corrected by observing the GIIRS's LW image and the 532nm atmospheric backscattering signal via the satellite observation telescope. The GLPS's Optical schematic diagram is shown in Fig. 3.

https://doi.org/10.5194/egusphere-2026-1163
Preprint. Discussion started: 3 July 2026


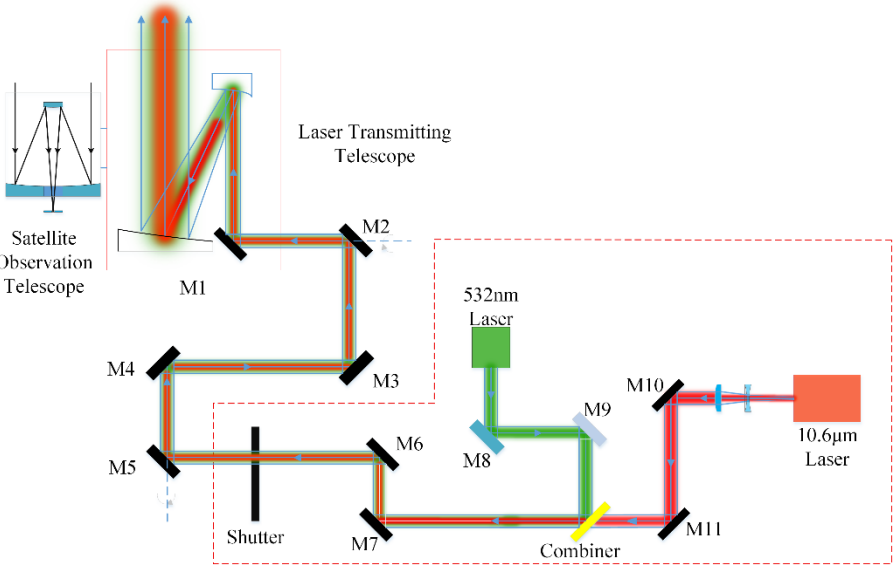


**Figure 3:** Optical schematic of the laser telescope.

The GLPS parameters have been carefully tailored to the specific characteristics of the GIIRS, guaranteeing that the laser signal will be detectable by its LW band. The parameters include the center wavelength of the laser, transmitting power, power stability, laser divergence angle, transmitting telescope aperture, pointing stability, and so on. The specific design values of these parameters are listed in Table 1.

**Table 2.** Main design values of GLPS's parameters.

| Content | Value |
|---|---|
| Center wavelength of the laser | 10.6 μm ± 0.1 μm |
| Transmitting power | Continuous Power: 300W |
| Power stability | 3% @1hour |
| Laser divergence angle | ≤300 μrad |
| Transmitting telescope aperture | 300 mm |
| Pointing stability | ≤10 μrad |

### 3.4 Pointing angle

According to the FY-4A orbit forecast data, the elevation and azimuth angles of the laser telescope can be accurately calculated at the specified observation time. The GLPS can automatically adjust the pointing angle and shoot to the FY-4A satellite. The elevation and azimuth angles are calculated as follows. First, the satellite position defined in the parallel equator geodetic coordinate (PEGC) is transformed into the earth centered earth fixed coordinate (ECEF):

$$R(X,Y,Z) = (\boldsymbol{EP} \times \boldsymbol{ER} \times \boldsymbol{GR}) \times r(x,y,z), \quad (1)$$

https://doi.org/10.5194/egusphere-2026-1163
Preprint. Discussion started: 3 July 2026


where r(x,y,z) represents the satellite position in PEGC, and R(X,Y,Z) is the transformed satellite position in ECEF. ***EP*** is the polar shift matrix, ***ER*** is the earth rotation matrix, and ***GR*** is the precession and nutation matrix. The relative position vector of the satellite and laser station in ECEF is calculated:

$$\Delta(\Delta x, \Delta y, \Delta z) = R(X, Y, Z) - R_A(X_A, Y_A, Z_A), \tag{2}$$

where $R_A(X_A, Y_A, Z_A)$ is the laser station position in ECEF. $\Delta(\Delta x, \Delta y, \Delta z)$ is the relative position vector of the satellite and laser station in ECEF. Two rotation matrix rotates the relative position vector to the local cartesian coordinate.

$$\Delta'(\Delta' x, \Delta' y, \Delta' z) = R_z(\mathrm{Lon}-180) \times R_y(\mathrm{Lat}-90) \times \Delta(\Delta x, \Delta y, \Delta z) \tag{3}$$

$$R_z(\theta) = \begin{pmatrix} \cos\theta & \sin\theta & 0 \\ -\sin\theta & \cos\theta & 0 \\ 0 & 0 & 1 \end{pmatrix}, \; R_y(\theta) = \begin{pmatrix} \cos\theta & 0 & -\sin\theta \\ 0 & 1 & 0 \\ \sin\theta & 0 & \cos\theta \end{pmatrix} \tag{4}$$

where Lon and Lat represent longitude and latitude degrees, respectively.

Then, the azimuth angle *Az* and elevation angle $E_l$ can be obtained as follows:

$$A_z = \arctan\left(\frac{\Delta' y}{\Delta' x}\right), \quad E_l = \arctan\left(\frac{\Delta' z}{\sqrt{(\Delta' x)^2 + (\Delta' y)^2}}\right) \tag{5}$$

## 4 The INV for FY-4A GIIRS using the GLPS

### 4.1 Satellite-ground integrated GLPS operation mode and workflow designs

#### 4.1.1 Satellite-ground Integrated Workflow

The workflow of the satellite-ground integrated task is shown in Fig. 4. The GLPS at laser stations is on standby for 7×24 hours and monitors the system status in real-time, such as transmitting power, telescope pointing angle, the operating temperature of the laser maser, the indoor and outdoor environment status of the laser station, and so on. According to the laser operation schedule, the GLPS performs a self-check first. Confirmed as correct, the azimuth and elevation angle pointing to the FY-4A is calculated according to the satellite orbit data.

https://doi.org/10.5194/egusphere-2026-1163
Preprint. Discussion started: 3 July 2026


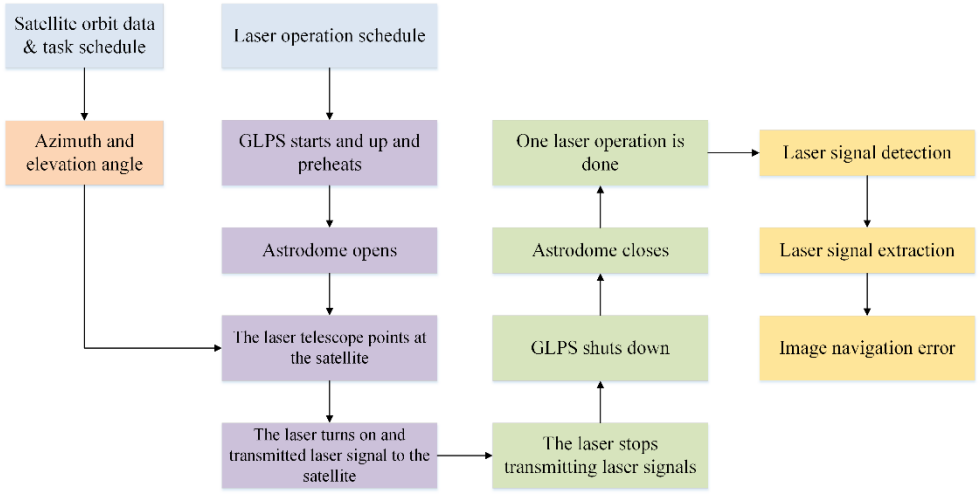


**Figure 4:** Satellite-ground Integrated workflow. The pale blue boxes indicate the files related to the FY-4A satellite. The purple boxes show the process of GLPS from start-up to transmitting laser signals. The orange box represents the calculated azimuth and elevation angle. The green boxes show the process of stopping transmitting laser signals to closing the dome. The golden boxes represent the procedure of image navigation error calculation.

According to the satellite task schedule, the GLPS starts up and preheats automatically. The dome opens, and the laser telescope points at the satellite according to the calculated azimuth and elevation angle. The GLPS transmits laser signal with the wavelength of 10.6 μm to the satellite. As the laser operation is over, the GLPS stops transmitting laser signals. The GLPS shuts down, and the astrodome closes. At this time, one laser mission has been completed, and the GLPS will be on standby, waiting for the next operation. Then, the image navigation error can be obtained with detecting and extracting the laser signal from the observed data.

#### 4.1.2 Satellite-ground Integrated Design of Observation Task

When the laser operations are scheduled, two different onboard observation modes, namely dwell observation and step scanning modes, are designed onboard. In dwell observation, the center of the detector array (i.e., No.48) is pointed toward the laser station, using its latitude and longitude as the imaging center. Under ideal conditions without navigation error, the laser spot should be centered on the central of No.48. In step scanning, GIIRS scans a line at a fixed 1/n step size, such as 1/2, 1/3, 1/4, or even 1/10 pixels. The entire step scanning would have (2n+1) columns and (2n+1) rows for a total of $(2n+1)^2$ scan locations. Fig.3 shows the 1/2 step scanning mode for the No.48 detector. As shown in Fig.5, the surrounding 3×3 neighbors with the No.48 detector as the center can be covered through 1/2 step scanning.

https://doi.org/10.5194/egusphere-2026-1163
Preprint. Discussion started: 3 July 2026


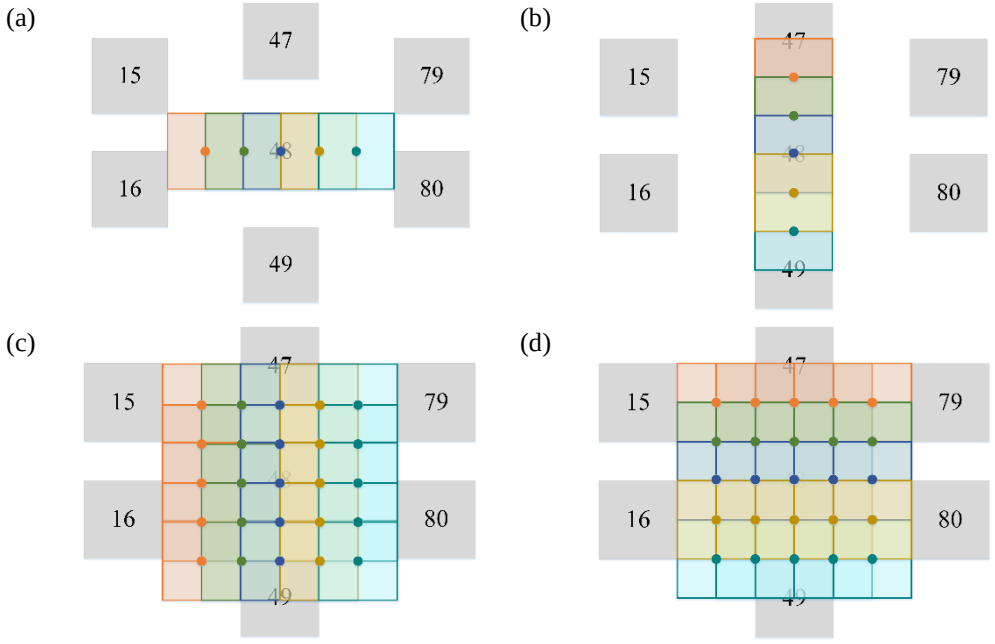


**Figure 5:** The diagram of 1/2 step scanning mode for No.48 detector. The entire step scanning task would have five columns and five rows for 25 scan locations. The square represents each scan location, and the dot with the same color as the square represents the center of this scan location. We use five colors representing five scan locations in a row or column. (a) the five scanning positions in the center column of five columns in the NS direction. (b) the five scanning positions in the center row of five rows in the EW direction. (c) the whole scan locations after stepping five columns in the NS direction. (d) the whole scan location after stepping five rows in the EW direction.

### 4.2 Methods

In theory, the GIIRS's LW band corresponding to the laser center wavelength is the default band, which is calculated as follows:

$$c_{laser} = \frac{(1/\lambda_{laser} - b_0)}{\Delta b} + 1 \quad (6)$$

where $\lambda_{laser}$ is the laser center wavelength, and $b_0$ is the first GIIRS band. $\Delta b$ is the spectral resolution, and $c_{laser}$ is the band number corresponding to the laser center wavelength.

#### 4.2.1 Detection of the laser signal

Ten nearest neighbors of $c_{laser}$ are used as the narrowed search range. A simple but efficient algorithm called laser index for laser signal detection is developed. For each detector, the laser index is calculated from the difference between the maximum and average value that removes the maximum and sub-maximum values. by comparing the laser index against a set of thresholds, the intensity of the laser signal can be divided into different levels, i.e., strong, weak, and no signal, respectively.

https://doi.org/10.5194/egusphere-2026-1163
Preprint. Discussion started: 3 July 2026


#### 4.2.2 Under dwell observation

Since 128 detectors are arranged into a 32×4 array with misalignments, the obtained LW data are discontinuous. To address this issue, the gray centroid method with the weighted matrix is applied to extract the deviation of the laser signal's center under the dwell observation. Owing to the 32×4 array configuration of the LW detector, has only one column of elements to its left. The relatively large inter-element spacing results to an extremely weak influence of the 5×5 neighborhood on No.48. Therefore, the distance between the center of No.48 and the center of its 3×3 nearest neighbor is calculated as the weight.

$$\mathbf{W}_x = \begin{bmatrix} d_x(D_{15}, D_{48}) & d_x(D_{47}, D_{48}) & d_x(D_{79}, D_{48}) \\ d_x(D_{16}, D_{48}) & 0 & d_x(D_{80}, D_{48}) \\ d_x(D_{17}, D_{48}) & d_x(D_{49}, D_{48}) & d_x(D_{81}, D_{48}) \end{bmatrix} \tag{7}$$

$$\mathbf{W}_y = \begin{bmatrix} d_y(D_{15}, D_{48}) & d_y(D_{47}, D_{48}) & d_y(D_{79}, D_{48}) \\ d_y(D_{16}, D_{48}) & 0 & d_y(D_{80}, D_{48}) \\ d_y(D_{17}, D_{48}) & d_y(D_{49}, D_{48}) & d_y(D_{81}, D_{48}) \end{bmatrix} \tag{8}$$

where $d_x(D_i, D_{48})$ and $d_y(D_i, D_{48})$ represent the distance between the center of No.48 and the center of No.$i$ in the $x$ and $y$ directions, respectively.

Then, the deviation of the laser signal's center compared to the center of No.48 can be obtained as follows:

$$x' = \frac{\sum_{i=1}^{3}\sum_{j=1}^{3} \mathbf{V}_{ij} \times \mathbf{W}_x}{\sum_{i=1}^{3}\sum_{j=1}^{3} \mathbf{V}_{ij}}, \; y' = \frac{\sum_{i=1}^{3}\sum_{j=1}^{3} \mathbf{V}_{ij} \times \mathbf{W}_y}{\sum_{i=1}^{3}\sum_{j=1}^{3} \mathbf{V}_{ij}} \tag{9}$$

where $x'$ is the deviation in the EW direction, and $y'$ is the deviation in the NS direction. In addition, $x'$ and $y'$ represent the image navigation accuracy as well.

#### 4.2.3 Under step scanning

Fig. 4 shows the established coordinate system, with its origin at the center of No 48. The x-axis is oriented along the EW direction (positive eastward), and the y-axis along the NS direction (positive northward).

https://doi.org/10.5194/egusphere-2026-1163
Preprint. Discussion started: 3 July 2026


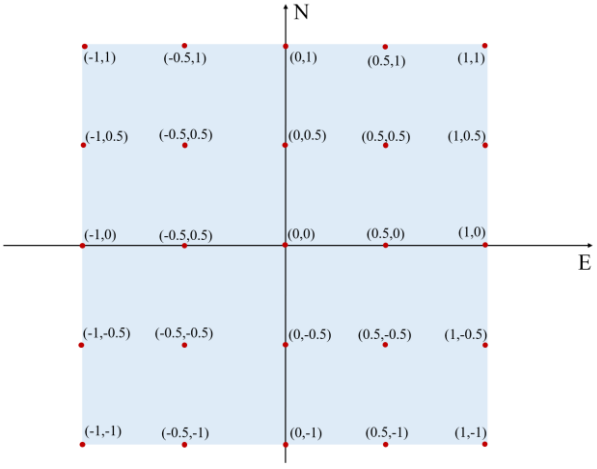


**Figure 6:** Diagram of the coordinate system under the 1/2 step scanning. In theory, the red dots and (x, y) are the locations and coordinates of 25 stepping positions.

Due to the misalignments on the GIIRS detector array and the cloud cover, the laser signals of $(2n+1)^2$ images may be discontinuous. Therefore, applying the interpolation method for the step scanning missions with discontinuous laser signals is very necessary. Here, the Kriging method is chosen to interpolate the discontinuous laser signals, which is widely acknowledged and applied as a powerful and efficient technique. It predicts values at unknown locations using values at known locations based on both mathematical functions and statistical theory, whose parameters are estimated based on spatial autocorrelation. Moreover, the randomness to approximate the variation present in geographic data is considered in the Kriging method.

Under the 1/2 step scanning mode, theoretically, only in the 13th step scanning position (the origin of the coordinates), the center of the laser spot is in the center of the detector, and the laser signal would be strongest. When the laser signals are discontinuous, after Kriging method, the coordinate position of the most significant laser signals in $(2n+1)^2$ images would be the subpixel deviation in the NS and EW direction.

## 5 Preliminary results and analysis

### 5.1 Data

Since the Jiamusi laser station was built in 2018, several laser observation experiments have been carried out so far. The Xinjiang laser station is newly built and we still have carried out two experiments. Based on these experiments, we carry out the following preliminary results and analysis.

https://doi.org/10.5194/egusphere-2026-1163
Preprint. Discussion started: 3 July 2026


### 5.2 Analysis of different performances for laser signal

The data obtained from the above experiments were analyzed via the laser index algorithm in this section. Fig. 7 presents the radiation values of 128 detectors' narrowed bands under different conditions. The maxband means the band in which the Maximum value of all Detectors in the narrowed search Range (MDR) is located. The maxband-1 means the previous band of the maxband, while the maxband+1 means the latter band of the maxband.

Fig. 7a shows the radiation value with no laser signals. When the laser signal is weak due to the influence of clouds, fog and the atmosphere in Fig. 7b, detecting the laser signal using the MDR would no longer be accurate. A strong laser signal would lead to an increase in the radiation value, as shown in Fig. 7c. In addition, as shown in Fig. 7c and d, the laser signal may cause more than one band's radiation value increase. It is necessary to eliminate the maximum value and sub-maximum value from the narrowed search range of a specific detector and then take the average value. The proposed laser index algorithm calculates the difference between the maximum and the average value that removes the maximum and sub-maximum from the narrowed bands, which can effectively avoid the problems mentioned above.

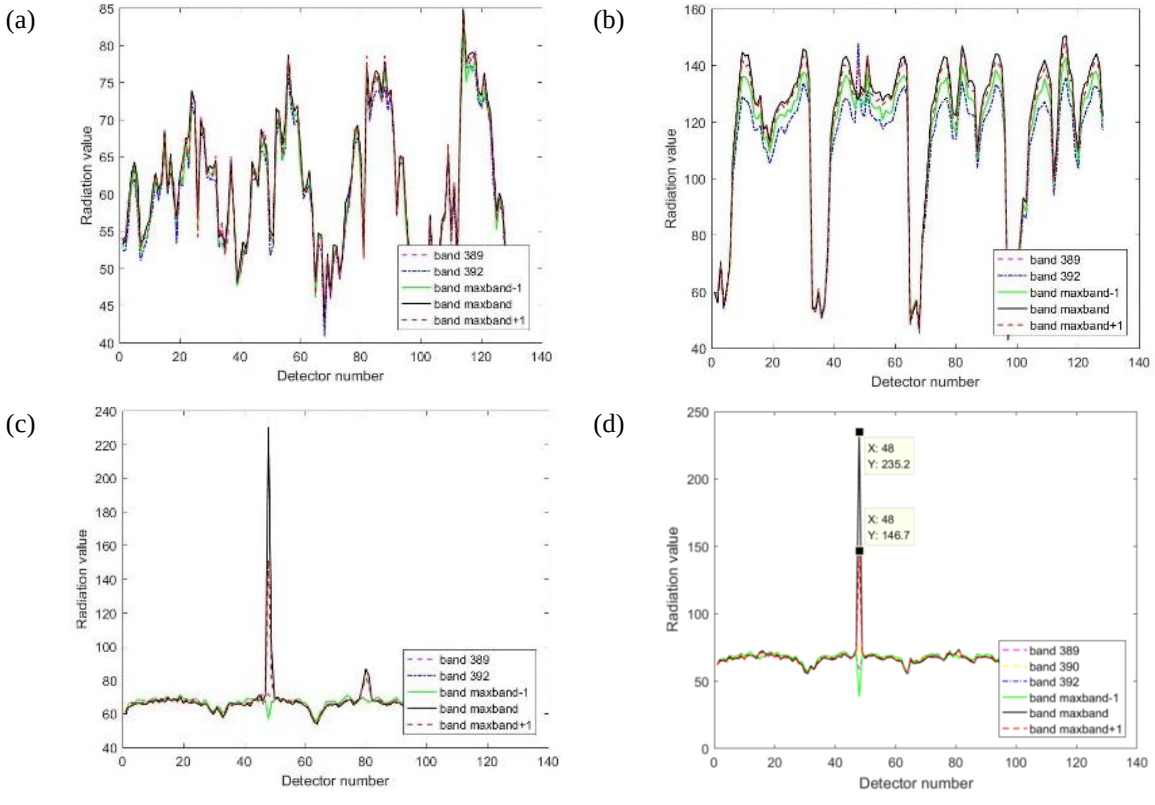


**Figure 7:** The radiation values of 128 detectors' narrowed bands are shown under different conditions. (a) no laser signal. (b) weak laser signal. (c) strong laser signal. (d) laser signal causes two bands to increase simultaneously.

https://doi.org/10.5194/egusphere-2026-1163
Preprint. Discussion started: 3 July 2026


### 5.3 Analysis of the Image Navigation Results using Dwell Observation Data

Fig. 8 shows the results calculated under the dwell observation at different times. Fig. 8a gives the calculated deviations of the whole mission. NS deviations are within 0.4 pixels by statistical analysis of all the missions, while EW deviations are within 0.2 pixels. The interval between adjacent detectors in EW direction is larger than that in NS direction, causing that the response of the adjacent detector in EW direction to the laser signal is weaker than that in the NS direction. The weighted matrix used in the gray centroid method is calculated using the distance between the center of No.48 and the center of its 3 ×3 nearest neighbour. Thus, the NS deviations are greater than EW deviations. Fig. 8b enumerates a set of similar statistics for the period of 01:00 and 05:00 UTC. The NS deviations are within 0.25 pixels, and EW deviations are within 0.03 pixels.

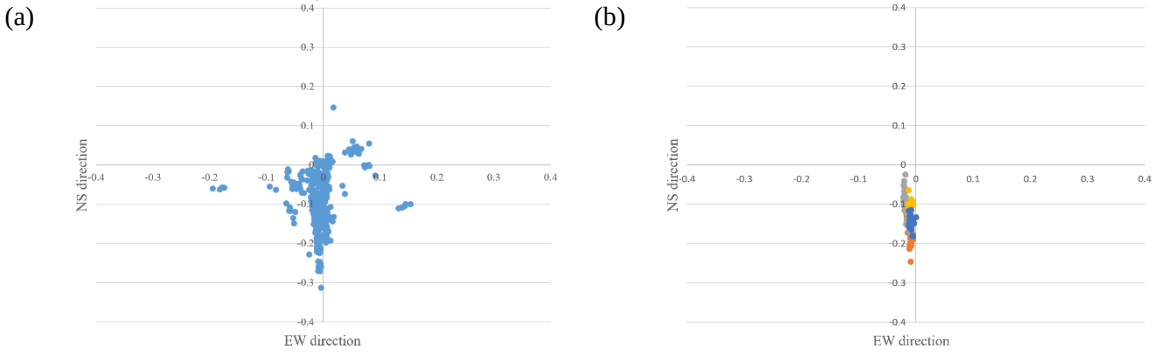


**Figure 8:** Results of image navigation under dwell observation. (a) the calculated deviations of the whole missions. (b) a set of similar statistics for the period of 01:00 and 05:00 UTC.

### 5.4 Analysis of the Image Navigation Results using Dwell Observation Data

Fig. 9 shows the results after interpolation under the step scanning at different times. According to the results of step scanning, the EW deviations are within 0.35 pixels, and NS deviations are within 0.45 pixels. In NS direction, the deviations of step scanning are consistent with those of the dwell observation. In EW direction, the deviations of step scanning are more precise than those of the dwell observation. This is due to the step scanning using a 1/n step size in the EW and NS direction, reducing the impact of a large interval between adjacent detectors in EW direction. When the laser signals are discontinuous, the location of the most potent laser can be found by interpolating the unknown laser signal. When the laser signal is powerful, the signal peak is pronounced. When the laser signal intensity is medium, there may be more than one signal peak but only one highest peak.

https://doi.org/10.5194/egusphere-2026-1163
Preprint. Discussion started: 3 July 2026


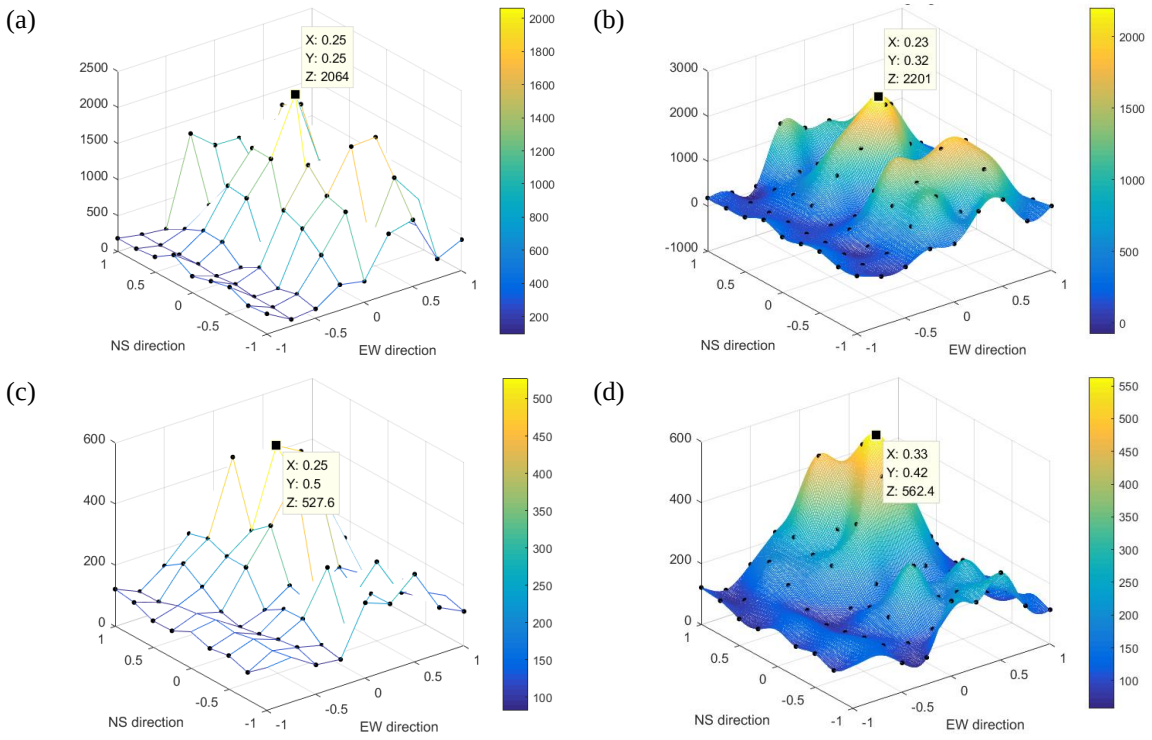


**Figure 9:** Results of image navigation performance under step scanning. (a)-(b) is the results of 3 pm on 26 April 2019 UTC, while (c)-(d) is the results of 1 pm on 25 April 2019 UTC. (a) (c) represents the interpolation results when the grid is 4. (b) (d) represents the interpolation results when grid is 100.

### 5.5 Comparing with the results of the visible band

To verify the reliability of INV using GLPS, the INV results using GLPS are compared with the results that of visible band. The navigation results of the visible band are evaluated through landmark registration. Since the resolution of the LW and visible band are different, the navigation deviation is converted from pixel to kilometers. The comparison results are listed in Table 3. From Table 3, The INV results of the two are nearly identical. The minor discrepancy is attributed to the separate and independent optical paths of the visible and infrared bands.

**Table 3.** The navigation results compared with the visible band's landmark.

| | LW with visible band | GLPS with LW band |
|---|---|---|
| EW | 7.2 km | 5.6 km |
| NS | 7.0 km | 7.2 km |

https://doi.org/10.5194/egusphere-2026-1163
Preprint. Discussion started: 3 July 2026


## 6 Conclusion

This work proposed the GLPS technique for GIIRS's LW INV. The GLPS is designed to precisely and automatically point at the satellite and transmits laser signals, whose center wavelength and energy can be detected by GIIRS's LW band. The result analysis of the laser data shows that GLPS is a reliable tool for INV. For the GIIRS's LW band, the preliminary results are that EW navigation deviations were within 0.35 pixels, and NS navigation deviations were within 0.45 pixels. Although this technique is only applied experimentally for the GIIRS LW band, it is useful for other instruments or channels. The GLPS for GIIRS MW band and LMI is under development. In the future, the multi-station joint validation of the geolocation accuracy will be carried out after the completion of the three laser stations, and provide valuable as well as precise results for further improvement of spaceborne instruments' INR.

***Acknowledgments.*** This work is supported in part by the National Key R&D Program of China under Grant 2021YFB3900400 and Grant 2021YFB3900402, in part by National Natural Science Foundation of China under Grant U2342201, in part by Youth Innovation Team, China Meteorological Administration (CMA2024QN10).

## References

Yang, J., Zhang, Z., Wei, C., Lu, F., & Guo, Q: Introducing the new generation of Chinese geostationary weather satellites, Fengyun-4. Bulletin of the American Meteorological Society, 98(8), 1637-1658, 2017.

Wang, X., Min, M., Wang, F., Guo, J., Li, B., & Tang, S.: Intercomparisons of cloud mask products among Fengyun-4A, Himawari-8, and MODIS. IEEE Transactions on Geoscience and Remote Sensing, 57(11), 8827-8839, 2019.

Grycewicz, T. J., Tan, B., Isaacson, P. J., De Luccia, F. J., & Dellomo, J.: Avoiding stair-step artifacts in image registration for GOES-R navigation and registration assessment. In Earth Observing Systems XXI (Vol. 9972, pp. 239-250). SPIE, 2016, September.

De Luccia, F. J., Houchin, S., Porter, B. C., Graybill, J., Haas, E., Johnson, P. D., ... & Reth, A. D.: Image navigation and registration performance assessment tool set for the GOES-R Advanced Baseline Imager and Geostationary Lightning Mapper. In Earth Observing Missions and Sensors: Development, Implementation, and Characterization IV (Vol. 9881, pp. 252-268). SPIE, 2016, May.

Emery, W. J., Baldwin, D., & Matthews, D.: Maximum cross correlation automatic satellite image navigation and attitude corrections for open-ocean image navigation. IEEE transactions on geoscience and remote sensing, 41(1), 33-42, 2003.

Yang, L., Feng, X., Guo, Q., Lu, F., & Zhang, X.: Automatic geometric precision correction of Fengyun-2 meteorological satellite imagery. Jisuanji Gongcheng yu Yingyong(Computer Engineering and Applications), 47(3), 2011.

Wang, W., Cao, C., Bai, Y., Blonski, S., & Schull, M. A.: Assessment of the NOAA S-NPP VIIRS geolocation reprocessing improvements. Remote Sensing, 9(10), 974, 2017.

https://doi.org/10.5194/egusphere-2026-1163
Preprint. Discussion started: 3 July 2026


Hou, S. Y., Qin, Z. Y., Niu, L., Zhang, W. G., & Ai, W. T.: A Landmark Matching Algorithm for the Geostationary Satellite Images Based on Multi-Level Grids. The International Archives of the Photogrammetry, Remote Sensing and Spatial Information Sciences, 42, 569-574, 2020.

Jiang, L., Li, X., Li, L., Yang, L., Yang, L., Hu, Z., & Chen, F.: On-orbit geometric calibration from the relative motion of stars for geostationary cameras. Sensors, 21(19), 6668, 2021.

Li, X., Yang, L., Su, X., Hu, Z., & Chen, F.: A correction method for thermal deformation positioning error of geostationary optical payloads. IEEE Transactions on Geoscience and Remote Sensing, 57(10), 7986-7994, 2019.

Tan, X., Yang, J., & Deng, X.: Filtering method of star control points for geometric correction of remote sensing image based on RANSAC algorithm. In Ninth International Conference on Graphic and Image Processing (ICGIP 2017) (Vol. 10615, pp. 1216-1221). SPIE, 2017, April.

Shang, J., Liu, C., Yang, L., Zhang, Z., & Wang, J.: Misalignment angle calculation accuracy analysis of three-axis stabilized geostationary satellite. Journal of Geoscience and Environment Protection, 5(12), 153, 2017.

Shang, J., Yang, L., Huang, P., Yang, H., Liu, C., Wang, J., ... & Zhang, Z.: Instrument observation strategy for a new generation of three-axis-stabilized geostationary meteorological satellites from China. Geoscientific Instrumentation, Methods and Data Systems, 8(2), 161-175, 2019.

Wang, J., Tong, X., Yang, L., Shang, J., Liu, C., Bao, S., ... & Yang, J.: Image navigation for FY-4A lightning mapping imager. IEEE Journal of Selected Topics in Applied Earth Observations and Remote Sensing, 14, 11450-11465, 2021.

Buechler, D., Varghese, T., Armstrong, P., Bremer, J., Lamb, R., Fulbright, J., & Goodman, S.: On-orbit validation of the geolocation accuracy of GOES-16 geostationary lightning mapper (GLM) flashes using ground-based laser beacons. In Earth observing systems XXIII (Vol. 10764, pp. 168-175). SPIE ,2018, September.